High-temperature thermophysical properties of γ- and δ-Mn from first principles

Hossein Ehteshami[1,*] and Andrei V. Ruban[1,2]

[1]*Department of Materials Science and Engineering, KTH Royal Institute of Technology, SE-10044, Stockholm, Sweden*
[2]*Materials Center Leoben Forschung GmbH, A-8700 Leoben, Austria*

Thermophysical properties of γ- and δ-Mn phases have been investigated using first-principles calculations in their thermodynamically stable temperature range. An adiabatic approximation is used for partitioning of the Helmholtz free energy into electronic, magnetic, and vibrational contributions from the corresponding temperature induced excitations, where the fastest degree of freedom has been included in the slower ones. Namely, electronic excitations (on a one-electron level) have been included directly in the first-principles calculations at the corresponding temperatures. Magnetic excitations in the paramagnetic state then have been taken into consideration in the two opposite limits: localized, considering only transverse spin fluctuations (TSF), and itinerant, allowing for the full coupling of transverse and longitudinal spin fluctuations (LSF). Magnetic contribution to the free energy has been included in the calculations of the vibrational one, which has been obtained within the Debye-Grüneisen model. The calculated thermophysical properties such as lattice constance, thermal lattice expansion, and heat capacity are in good agreement with available experimental data, especially in the case when the itinerant magnetic model is chosen. We also present our results for elastic properties at high temperatures.

I. INTRODUCTION

Elemental Mn has been in the focus of scientific and industrial research communities because of its complex crystal structures and its usage as an alloying element in a wide spectrum of different materials. It has a very rich crystallographic and magnetic phase diagram. The low temperature phase of Mn, α-Mn, containing 58 atoms in the unit cell (space group $T_d^3 - I\bar{4}3m$), is considered the most complex structure of elemental solids.

Among five allotropic forms of Mn, four have cubic symmetry in their thermodynamic stability temperature range. An exception to this rule is α-Mn, which has a tetragonal distortion below Néel temperature T_N of 95 K with $c/a = 0.99955$ [1] where a noncollinear antiferromagneticlike order is formed. A theoretical study by Hobbs *et al.* [2] shows that a magnetic frustration on inequivalent sites of MnIV drives the magnetic structure to become noncollinear.

The α phase is stable up to 1000 K where it transforms to β-Mn. The β phase has a simple cubic structure with 20 atoms in the unit cell (space group $P4_132$). It is thermodynamically stable between 1000 K and 1368 K. Geometric frustration plays a crucial role in this phase which also causes a lack of any kind of magnetic order down to very low temperature. Experimental evidence for the existence of sizable local moments on MnII sites has led researchers to anticipate that the β phase is a 'quantum spin liquid' at low temperatures [3].

Above 1368 K, the β phase transforms to the fcc γ-Mn, which remains stable up to 1406 K where it transforms again to the bcc δ-Mn, stable up to the melting point T_M 1517 K.

Experimental investigations of these phases at high temperature are extremely difficult. Therefore, different approaches are used to stabilize them at low temperatures. In the case of γ-Mn, alloying with Ni, Cu, or Pd with consequent quenching to low temperatures allows one to get stable γ-Mn. Then the desired properties of γ-Mn can be obtained by studying their concentration dependence with decreasing amount of alloying elements.

Employing this method, Endoh and Ishikawa [4] studied magnetic and structural properties of quenched γ-FeMn by means of neutron diffraction. They found that γ-Mn is tetragonally distorted below the Néel temperature T_N 540 K where antiferromagnetic type I (AFMI) ordering causes a tetragonal distortion leading to $\approx 6\%$ contraction of the unit cell along the [001] axis. A magnetic moment of 2.3 μ_B extrapolated to 0 K has been reported in their study. This magnetically assisted tetragonal distortion was first investigated by Oguchi and Freeman [5] using first-principles method whose results were in good agreement with the experimental data [4]. Thermal properties of γ-Mn, e.g., heat capacity and thermal expansion were also determined from an extrapolation of the data for γ-MnCu alloys [6].

Since alloying and subsequent quenching was not possible for δ-Mn, an epitaxial growth was used to study properties of the δ phase, which was grown on different bcc substrates such as Cr, Fe, or V. The main difficulty in such studies was a strain induced by a substrate, which might cause a substantial deviation of the properties of a thin layer from those of the bulk. The effect of substrate on magnetic properties of thin films of Mn has been a matter of thorough discussion in the literature [7].

Early first-principles calculations within the local density approximation (LDA) for the fcc [8] and bcc Mn [9] suggested

*heht@kth.se

that there should be an almost degeneracy between energy of nonmagnetic (NM) and AFMI states at the equilibrium (LDA) volume. These calculations also predicted an AFM structure for the expanded experimental volume. Later generalized gradient approximation (GGA) calculations by Asada and Terakura [10] and Eder *et al.* [11] removed the degeneracy between the NM and AFMI states in fcc Mn and the NM and ferromagnetic (FM) states in bcc Mn predicted within the LDA. They found that the AFMI is the ground state of fcc Mn. At the same time, they disagreed on the magnetic ground states of the bcc Mn: While Asada and Terakura [10] predicted that it is FM, Eder *et al.* [11] found the AFMII state to be the magnetic ground state of the bcc Mn.

The latest calculations for the bcc and fcc structures were reported by Hafner and Hobbs [12] who used an all-electron projector-augmented wave (PAW) method to study different phases of Mn. The AFMI state is found to be the magnetic ground state of the fcc Mn and the AFMII state the magnetic ground state of the bcc Mn. For bcc Mn, they also reported that first-order transition from the AFMII to the AFMI state at $\approx 1.23\%$ expanded volume.

The earlier prediction [13] that the ground state of bcc Mn is a ferrimagnetic (FIM) state has been argued by Monh *et al.* [14] who have shown that the FIM is just projection of a spin-spiral state onto a collinear spin-quantization axis. Several spin-spiral states have been reported in that study [14], which might represent the ground state depending on the volume.

Although there exist numerous investigations of the magnetic ground state of bcc and fcc Mn at 0 K, theoretical calculations for high temperature γ and δ phases are absent. The only published attempt to study such phases at finite temperature is Asada and Terakura's work where they used a quasiharmonic approximation to study competing phases below T_N. In their study, the Debye-Grüneisen model (DGM) was set up following a semiemprical Moruzzi, Janak, and Scharwz (MJS) scheme [15]. The cohesive energy curves computed at 0 K of each phase were used to calculate the Debye temperature. It was mentioned that the reason why the Grüneisen constant came out negative for the AFMI bcc Mn was an abnormally flat cohesive energy curve.

Because of difficulties in performing high temperature experiments, there is no experimental data for elastic moduli of γ and δ-Mn. The available data usually corresponds to highly concentrated alloys and in a temperature range much lower than the thermodynamically stable range of these phases. Theoretical calculations for elastic properties of paramagnetic γ and δ-Mn are also lacking. This could be partly due to a rather large underestimation of the lattice parameter obtained from first-principles calculations. It has been suggested that an underestimation of the lattice parameter in γ-Mn could be due to strong correlation effects in this system [16] although taking such effects into consideration does not improve results much compared to the GGA calculations [11].

Several strategies have been put forward by different groups to study finite temperature properties of elements and alloys such as thermodynamic integration [17–20] and temperature dependent effective potentials [21,22]. While both techniques are powerful and proven to be successful in many applications, they are computationally expensive and may have problems related to structural stability of investigated phases.

For example, a recent application [23] of TU-TILD thermodynamic integration [24] for δ-Mn overestimated the heat capacity by 9.3 J/mol K at 1514 K, near to the melting point. A technical difficulty that has been observed for such simulations is that δ phase is dynamically unstable at lower temperatures and therefore transforms to ω phase. Transformations of this kind demand a special care for thermodynamic modeling of high temperature phases. Besides, the above mentioned techniques are not able to take properly into consideration thermal magnetic excitations, which play a crucial role in thermodynamic properties of these systems as will be demonstrated below.

In the present paper, we use therefore another approach to the calculations of thermophysical properties of γ and δ-Mn at high temperatures. Following the coarse-graining of the partition function in time scale, we first include the one-electron excitations in the first-principles calculations. Simultaneously, we include in our first-principles calculations magnetic excitations in the paramagnetic state in two two different limits: either including only TSF or fully coupled TSF and LSF. These excitations are then adiabatically coupled to the thermal lattice vibrations calculated within the Debye-Grüneisen model.

II. METHODOLOGY

A. Electronic structure calculations

Density functional [25] calculations in this work have been performed by the exact muffin-tin orbital (EMTO) method [26–28] within the coherent potential approximation (CPA) [29,30] for the electronic structure of the disordered local moment (DLM) atomic spin configuration (an alloy consisting of 50% spin-up($\uparrow$) and 50% spin-down($\downarrow$) used to model a paramagnetic state [31,32].

The total energies have been calculated using GGA [33,34] using the full charge density (FCD) technique [28,35]. The EMTO-CPA calculations were done using an orbital momentum cutoff $l_{max} = 3$ for partial waves. The integration of the Brillouin zone was performed using $27 \times 27 \times 27$ for γ-Mn and $33 \times 33 \times 33$ for δ-Mn k-point grids generated according to the Monkhorst-Pack scheme [36].

B. Helmholtz free energy calculations

In this study, the Helmholtz free energy F is obtained by its partition to different contributions [37–39] and using adiabatic approximation to connect different parts to each other. In this approximation, the renormalization of electronic structure due to atomic vibration is absent, i.e., it is a static lattice approximation. Effects beyond static lattice can be important in particular systems [19,40]. Nevertheless, as will be shown, the static lattice method is still a good approximation when one compares the results with experiments.

The total free energy is divided into two major contributions $F = F_E + F_V$: partial free energy F_V due to *slower* atomic vibrations and partial free energy F_E due to *faster* electronic and magnetic excitations. Following the adiabatic assumption, the vibrational partial free energy F_V is calculated using the DGM based on F_E electronic partial free energy, which also include magnetic contributions through an additional modeling
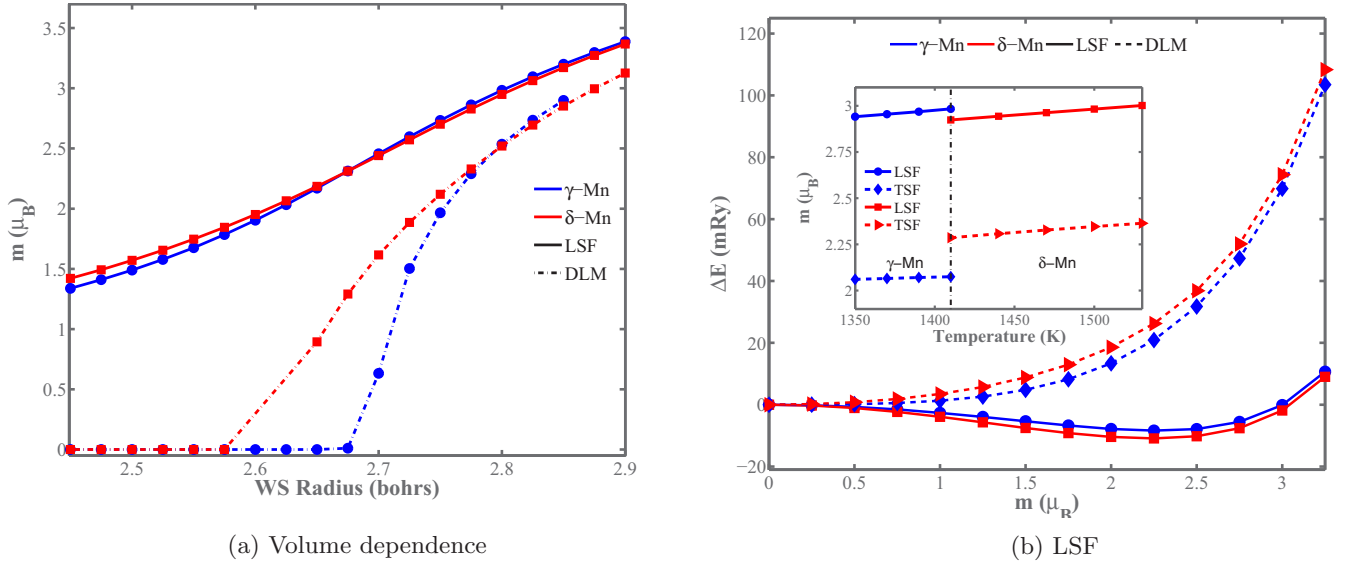
(a) Volume dependence

(b) LSF

FIG. 1. (a) Volume dependence of magnetic moments calculated using different models. For LSF data calculations have been done at 1410 K and for DLM at 0 K. (b) Longitudinal spin fluctuations energy as a function of magnetic moments μ_B. LSF curve represents the energy calculated at 1410 K and for Wigner-Seitz radius of 2.80 bohrs and DLM curve shows the energy at 0 K and for Wigner-Seitz radius of 2.60 bohrs. Inset: temperature dependence of magnetic moments for γ- and δ-Mn. Moments calculated at theoretical equilibrium volumes.

of the corresponding magnetic state. The contribution from one-electron excitations is calculated by using the Fermi-Dirac function in the electronic structure calculations [41].

C. Magnetic excitations

In both structures, Mn is in the paramagnetic state in the corresponding temperature range. The simplest description of that state is given by the DLM model, which takes into account only transverse spin fluctuations [42]. High-temperature transverse fluctuations correspond to a Heisenberg type paramagnetic gas with local spin moments S, whose entropy is $k_B \ln(2S+1)$. In our case $2S = m$, where m is the local magnetic moment of an atom. Therefore, the magnetic entropy is given by the usual formula [43,44]:

$$S^{\text{TSF}} = k_B \ln(m+1), \tag{1}$$

where m is the magnetic moment obtained in self-consistent DLM-CPA calculations.

It is applicable, however, only in the case when local magnetic moments are large and stable with respect to perturbations of the magnetic state. In Fig. 1(a), we show the dependence of the local magnetic moments of the γ and δ phases on the Wigner-Seitz radius in the DLM state in the 0 K DLM-CPA calculations. As one can see, the local magnetic moments practically vanish in both phases for the equilibrium 0 K lattice parameter. One can also see that the LSF energy presented in Fig. 1(b) has nearly parabolic form.

This is a clear indication of the itinerant character of magnetism in these two phases. Therefore, in order to include LSF in our calculations, we use an approximate expression for the magnetic entropy with the full coupling of the transverse and longitudinal fluctuations [45]

$$S^{\text{LSF}} = 3k_B \ln(m). \tag{2}$$

Here m is the average magnitude of the local magnetic moment, which should be determined self-consistently by minimizing the corresponding Helmholtz free energy. This expression is valid in the classical limit if the LSF energy has a quadratic form, although it also produces quite reasonable results for a more complicated form of the LSF energy, similar to those presented in Fig. 1(b) for larger equilibrium high-temperature Wigner-Seitz radii. Although in the latter case the LSF energy has a more complicated form with a minimum at higher magnitudes of the local magnetic moment, the difference between LSF energy minimum and LSF energy for $m = 0$ is of an order of 8 mRy, i.e., ≈ 1260 K, which is less than the temperature of interest and thus LSF should play an important role also in this case.

D. Free energy of lattice vibrations

The vibrational free energy contribution $F_V = E_D - T S_D$ is calculated using DGM where

$$E_D(V,T) = \tfrac{9}{8}\Theta_D + 3k_B T D(\Theta_D/T), \tag{3}$$

$$S_D(V,T) = k_B[4D(\Theta_D/T) - 3\ln(1 - e^{-\Theta_D/T})]. \tag{4}$$

Here $D(x) = (3/x^3)\int_0^x dt[t^3/(e^t - 1)]$ is the Debye function. The Debye temperature $\Theta_D(V,T)$ was determined from the *mean* sound velocity $v_m(V,T)$, namely:

$$\Theta_D = \frac{\hbar}{k_B}\left(\frac{6\pi^2}{V}\right)^{1/3} v_m(V,T). \tag{5}$$

The mean sound velocity must be calculated by averaging the three acoustic branches over directions confined to the first Brillouin zone, viz.:

$$v_m(V,T) = \left(\frac{1}{3}\sum_{i=1}^{3}\int_\Omega \frac{1}{v_i^3}\frac{d\Omega}{4\pi}\right)^{-\frac{1}{3}}, \tag{6}$$

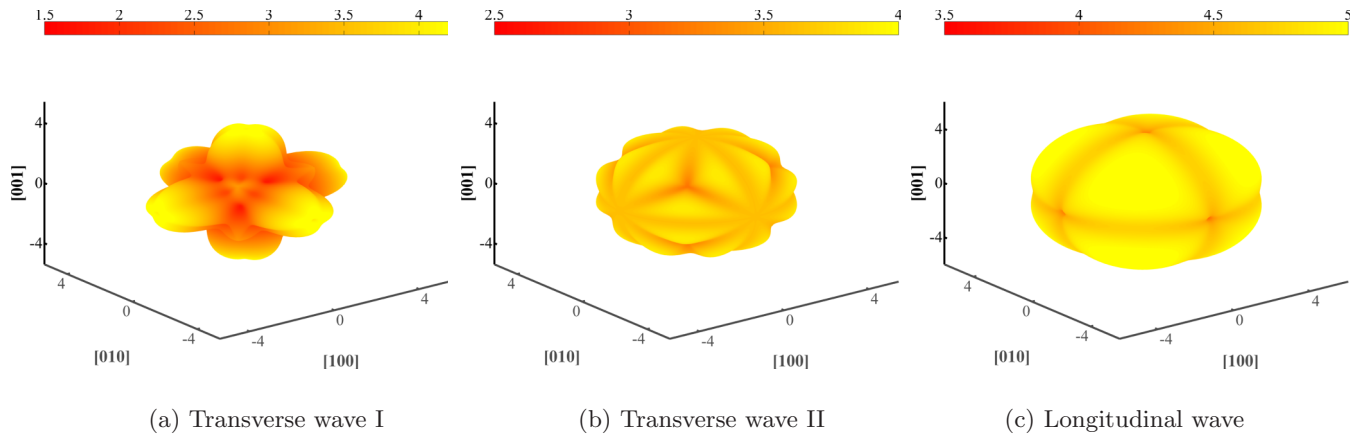(a) Transverse wave I (b) Transverse wave II (c) Longitudinal wave

FIG. 2. Group velocities (km/sec) of δ-Mn as a function of crystallographic direction. The calculated velocities correspond to Wigner-Seitz radius of 2.775 bohrs at 1440 K. The unit of color legend is km/sec.

where $d\Omega$ is an increment of the solid angle about the center of the Brillouin zone, and v_i's are longitudinal and transverse sound velocities. It is desirable to find some approximations for Eq. (6) in order to simplify the calculations. For example, for isotropic crystals [46] this relation simplifies to:

$$v_m = \left(\frac{1}{3} \left[\frac{2}{v_s^3} + \frac{1}{v_l^3} \right] \right)^{-\frac{1}{3}}, \qquad (7)$$

where v_s and v_l are transverse (shear) and longitudinal sound velocities, respectively. In an isotropic solid, two transverse velocities are considered to be degenerate. As we shall observe, it is hardly the case for a real crystal.

E. Debye temperature calculations

The MJS model [15] suggests a semiempirical relation between bulk modulus and Θ_D. This approximation has been successfully applied in many DGM investigations of different systems including quite complex ones [48]. However, its success has a limitation as has been pointed out, for example, in the case of δ-Fe [49]. A common practice is to use homogenization theories such as Voight, Reuss, or Hill averages to relate the single crystal elastic constants to the mean sound velocities. In such cases, an isotropic propagation of sound velocities is assumed and Eq. (7) will be used to calculate Θ_D. Since there are several choices to evaluate the averaged sound velocity from the single crystal elastic constants, a legitimate question can be raised: Which of the homogenization theories is the most appropriate one?

For an example, Ledbetter [50] has employed different homogenization theories for different elements and reported that Reuss's method, which assumes uniform local stress, is a better approximation than Voight's method, which assumes uniform local stress. Ledbetter's argument is based on the fact that continuity of stress across grains that comes from Reuss's approximation is more important than the strain continuity that comes from Voight's approximation. Our calculations based on Voight and Reuss approximations show that this is certainly not true, for example, in the case of γ-Mn.

Therefore we directly calculate the averaged sound velocity from Eq. (6). The directions confined to the irreducible wedge of the Brillouin zone for both γ and δ phases have been sampled and for each direction, the group velocities are calculated by solving the Christoffel equation [51]. Once the directional dependence of velocities is known, one can directly obtain the average sound velocity v_m using Eq. (6). Calculated sound velocities using the direct averages are almost identical to an approximation introduced recently, the resultant effective direction (RED) technique [49]. Since elastic constants are temperature and volume dependent, the procedure mentioned above is repeated for each volume and temperature in order to calculate $v_m(V, T)$. The calculations of the single-crystal elastic constants from partial free energies will be discussed in Sec. III C.

The three group velocities can be seen in Fig. 2 as a function of reciprocal direction. Although for general directions the vibrational modes are not strictly pure transverse or longitudinal [52], they have been categorized here in this way for the sake of convenience. It can be seen in Fig. 2(a) that the lowest shear shows a very anisotropic behavior. The same is true for the next shear mode which can be seen in Fig. 2(b). These two modes play a crucial role in determination of v_m as can be understood from Eq. (6). On the other hand the longitudinal mode, Fig. 2(c), shows an isotropic behavior which is a rather expected behavior for this type of mode.

When the v_m and consequently Θ_D is calculated as a function of volume and temperature, the vibrational energy E_D and entropy S_D can be evaluated together with the total free energy

$$F(V, T) = F_E(V, T) + E_D(V, T) - T S_D(V, T).$$

The fitted total free energy $F(V, T)$ is then used to calculate the thermophysical properties namely lattice constant $a(T)$, linear thermal expansion coefficient (TEC) α, and isobaric heat capacity $C_p(T)$ using appropriate derivatives of the free energy. Elastic moduli and isothermal bulk modulus B_T have been computed from the electronic partial free energies $F_E(V, T)$ at the theoretical equilibrium volume.
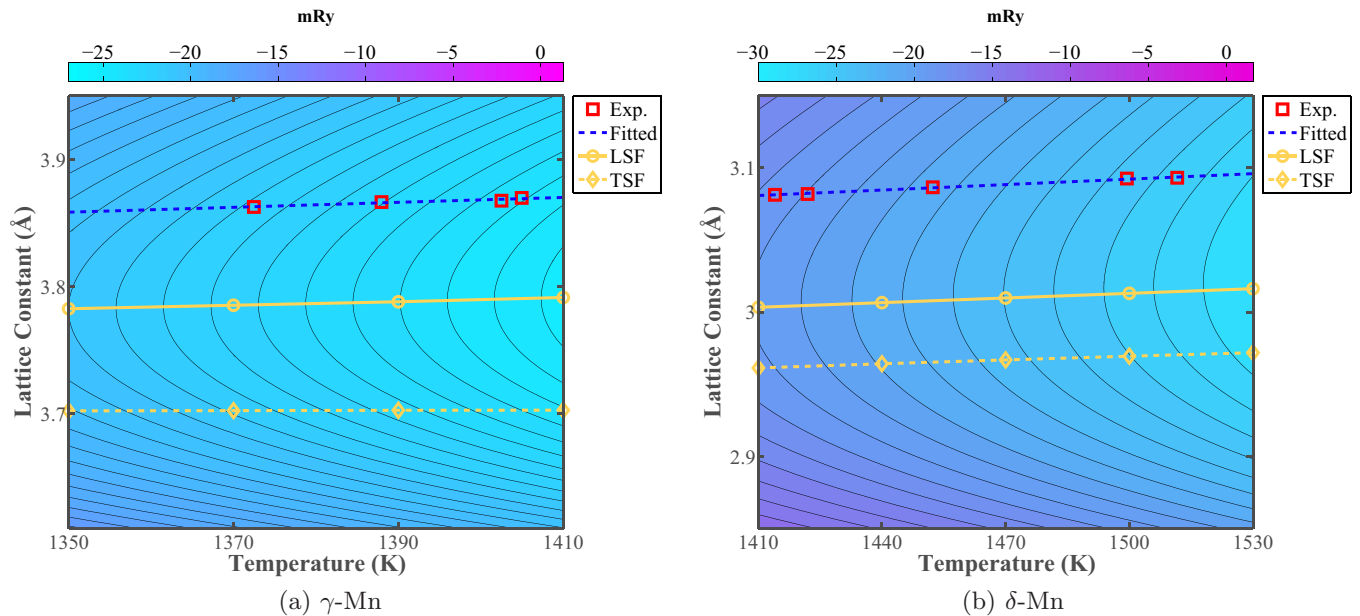
FIG. 3. Calculated temperature dependence of the lattice parameter for (a) γ- and (b) δ-Mn. The background of both panels is the contour plot of the Helmholtz free energy as a function of temperature and lattice constant. The unit of color legends is mRy. Experimental data are taken from Ref. [47].

III. RESULTS

A. Thermal lattice expansion

The calculated lattice parameter as a function of temperature is shown in Fig. 3(a) for γ-Mn and Fig. 3(b) for δ-Mn. It is somewhat underestimated for both phases and in both TSF and LSF calculations compared to the experimental data of Ref. [47]. However, the LSF results for the lattice constant, which are 2.0% below the experimental data, are in better agreement than the TSF results, which are about 4% lower.

The temperature dependence of the lattice constant is also better reproduced by the LSF model as can be seen in Fig. 3(b) and in Table I where the thermal expansion coefficient (TEC) is presented. As one can see, although the LSF model somewhat underestimates the TEC for both phases compared with experimental data [47], the TSF model completely fails to produce reasonable results for γ-Mn, which is known to have the largest TEC among all the fcc transition metals and alloys in the $3d$ series [6]. According to our results, this is due

TABLE I. Calculated and experimental linear TEC of γ- and δ-Mn. All the data are in 10^{-6} K^{-1} units and have been averaged over the temperature range of stability of the corresponding paramagnetic phase.

		TSF[a]	LSF[b]	Experiment[c]
γ-Mn:	Total	2.74	38.42	49.72
	El.+mag.[d]	10.88	24.62	
δ-Mn:	Total	29.67	35.71	40.84
	El.+mag.[d]	5.87	24.45	

[a]Calculated with longitudinal spin fluctuations (LSF) model.
[b]Calculated with longitudinal spin fluctuations (TSF) model.
[c]Lattice parameter measurements, Ref. [47].
[d]Expansion due to electronic and magnetic excitations.

to large negative contribution from lattice vibrations within this model. This surprising result is due to an anomaly in the elastic constants in the TSF model, which will be discussed in Sec. III C.

It is also clear from Table I that the electronic and magnetic contributions to the TEC are dominating in the LSF model, making up more than 60% of the total TEC. These contributions are significantly reduced in the case of the TSF model, especially in δ-Mn. Quite poor results obtained within the TSF model for the lattice constant and the TEC are related to the total neglect of longitudinal spin fluctuations at high temperatures, which increase the magnitude of the local moment affecting thereby the equilibrium lattice constant at the corresponding temperature.

B. Heat capacity

Figure 4(a) shows a variation of the heat capacity for γ and δ-Mn with temperature. A decomposition of the heat capacity into various contributions have been also presented in Fig. 4(a). The assessed experimental data by Desai [53] is plotted by black lines for the sake of comparison. In Desai's work, the available experimental data for the heat capacity have been analyzed considering thermodynamic consistency and reported. Thus they can be viewed as the most reliable values available for the heat capacity. Hereafter, we denote the values reported by Desai as experiment.

In Fig. 4(a), we observe that the heat capacity C_p has been underestimated for both γ and δ-Mn. For γ-Mn at 1410 K, the heat capacity in the LSF calculations is underestimated by 4.5% with respect to the experimental value and by 4.4% at 1360 K. On the other hand, the heat capacity of γ-Mn predicted in the TSF calculations is underestimated by 27% at 1360 K and 28% at 1410 K. The C_p of δ-Mn obtained in the LSF and TSF calculations is underestimated by 8% and 16% at 1410 K, respectively. Thus, the LSF model reproduces rather
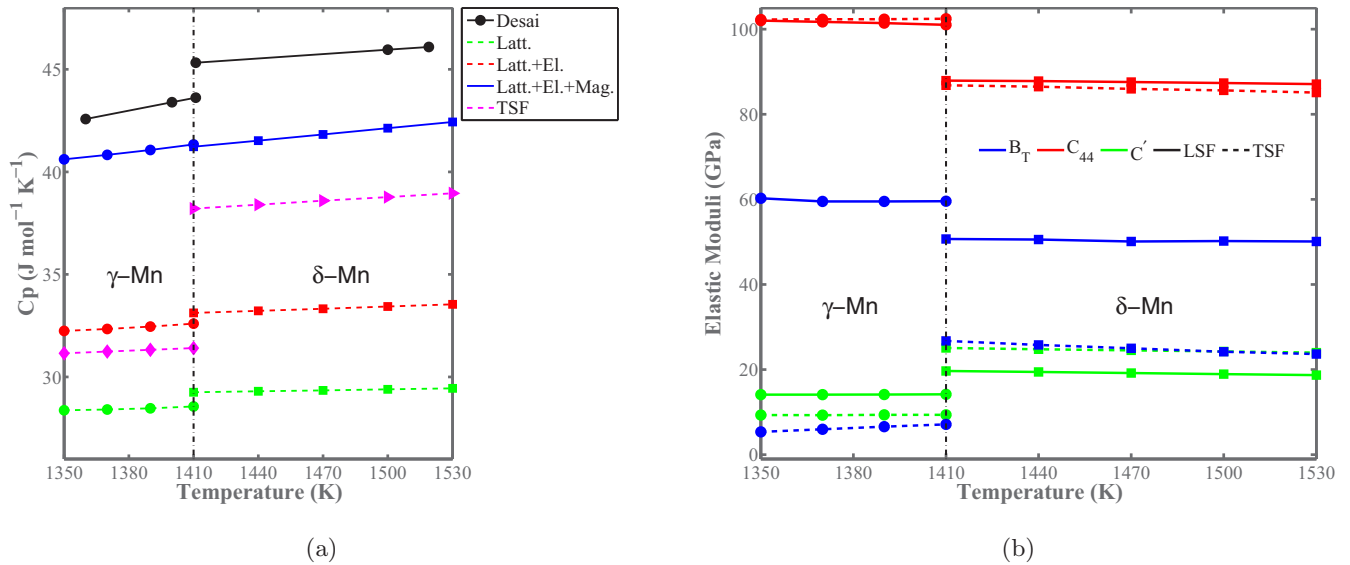
(a)

(b)

FIG. 4. (a) Calculated heat capacity C_p and its contributions as a function of temperature. Desai's work [53] represents the critically assessed values of a large set of experiments. (b) Calculated temperature dependence of elastic moduli of γ- and δ-Mn. Blue, red, and green lines represent the variation of B, C_{44}, and $C_{\prime}$, respectively.

well different sets of experiments for the lattice constant and heat capacity in both phases.

Table II shows C_p and C'_p obtained by different methods. Let us note that the calculated value of C_p using the TU-TILD method at 1410 K overestimates C_p by 5.47% and by 21% at 1520 in δ-Mn, which results in a huge slope of the heat capacity, not observed experimentally. Highly overestimated value of C'_p implies high compliance of the lattice and therefore quite high values of TEC.

The TSF calculations fail to reproduce C'_p in γ-Mn although they yield reasonable results for δ-Mn. The LSF model, on the other hand, gives a better value of C'_p for γ and slightly overestimated C'_p for δ-Mn. Nevertheless, the LSF model definitely provides much better overall description of the thermodynamic properties of both γ and δ phases.

C. Elastic properties

There are three independent elastic constants for cubic lattices. In addition to the bulk modulus, one needs to evaluate

TABLE II. Calculated and assessed experimental C_p γ- and δ-Mn. Data for C_p are in J (mol K)$^{-1}$ and for $\frac{dC_p}{dT}$, slope of heat capacity are in Jmol^{-1} K^{-2} $\times 10^{-3}$ units and have been averaged over the temperature range of stability of the corresponding paramagnetic phase.

		TSF[a]	LSF[b]	Theory[c]	Desai[d]
γ-Mn:	1360 K	31.20	40.72		42.58
	C'_p	4.27	12.22		20.49
δ-Mn:	1500 K	38.77	42.13	54.33	45.96
	C'_p	6.20	10.07	70.92	7.13

[a]Calculated with longitudinal spin fluctuations (LSF) model.
[b]Calculated with longitudinal spin fluctuations (TSF) model.
[c]TU-TILD method, Ref. [23].
[d]Assessed experimental heat capacity of Ref. [53].

two more elastic constants to determine all of them. Here, we have determined C_{44} and $C' = (C_{11} - C_{12})/2$ by applying a homogeneous lattice distortion at a fixed volume and calculating the electronic and magnetic partial free energy, similar to the previous studies [49,54].

In Fig. 4(b), we show the elastic constants as a function of temperature obtained at the corresponding theoretical equilibrium volume. As one can see, they change very little (less than 1%) in the corresponding temperature range. The bulk modulus of γ-Mn calculated using the TSF model is anomalously low and, surprisingly, it increases with temperature. This is because of an anomaly in volume dependence of the bulk modulus.

According to the TSF results, there is a plateau in volume dependence of the bulk modulus that follows with an increase with the increase of volume. The volume dependence of elastic constants C' obtained using the TSF model shows also an anomalous behavior similar to the bulk modulus. Moreover, the bulk modulus predicted by the TSF model is almost identical to the value of C' for both phases.

Such an unphysical behavior of elastic moduli within the TSF model is an indication that it does not work properly for γ-Mn. On the contrary, the LSF model provides a much more reasonable description of the elastic properties, although the bulk modulus calculated using the LSF model is also rather low. The difference in calculated C' using the LSF and TSF models is also appreciable when one takes into account the fact that this modulus is small.

On the other hand, C_{44} elastic modulus seems to be insensitive to the type of the used magnetic model: Both models give similar results. Unfortunately, there is no experimental information about elastic properties of γ-Mn and δ-Mn. Nonetheless, considering the results of the previous sections it seems likely that the LSF results could provide a better description for elastic moduli.

IV. CONCLUSIONS

High-temperature thermophysical properties of γ- and δ-Mn have been calculated by means of first-principles modeling of the free energy in the paramagnetic state. The latter has been described using the TSF and LSF models based on the DLM-CPA description of the electronic structure. The results show that the LSF model agrees much better with the available experimental data such as lattice constants, thermal expansion, and heat capacity. Our results show that the LSF have pronounced effect on all the calculated properties, and therefore they should be taken into consideration in the corresponding modeling of these phases.

[1] A. C. Lawson, A. C. Larson, M. C. Aronson, S. Johnson, Z. Fisk, P. C. Canfield, J. D. Thompson, and R. B. V. Dreele, J. Appl. Phys. **76**, 7049 (1994).

[2] D. Hobbs, J. Hafner, and D. Spišák, Phys. Rev. B **68**, 014407 (2003).

[3] H. Nakamura, K. Yoshimoto, M. Shiga, M. Nishi, and K. Kakurai, J. Phys.: Condens. Matter **9**, 4701 (1997).

[4] Y. Endoh and Y. Ishikawa, J. Phys. Soc. Jpn. **30**, 1614 (1971).

[5] T. Oguchi and A. J. Freeman, J. Magn. Magn. Mater. **46**, L1 (1984).

[6] M. Acet, H. Zähres, W. Stamm, E. F. Wasserman, and W. Pepperhoff, Physica B **161**, 67 (1990).

[7] J. Hafner and D. Spišák, Phys. Rev. B **72**, 144420 (2005).

[8] V. L. Moruzzi, P. M. Marcus, and J. Kübler, Phys. Rev. B **39**, 6957 (1989).

[9] J. Kübler, J. Magn. Magn. Mater. **20**, 107 (1980).

[10] T. Asada and K. Terakura, Phys. Rev. B **47**, 15992 (1993).

[11] M. Eder, J. Hafner, and E. G. Moroni, Phys. Rev. B **61**, 11492 (2000).

[12] J. Hafner and D. Hobbs, Phys. Rev. B **68**, 014408 (2003).

[13] V. L. Moruzzi and P. M. Marcus, Phys. Rev. B **38**, 1613 (1988).

[14] P. Mohn, K. Schwarz, M. Uhl, and J. Kübler, Solid State Commun. **102**, 729 (1997).

[15] V. L. Moruzzi, J. F. Janak, and K. Schwarz, Phys. Rev. B **37**, 790 (1988).

[16] I. D. Marco, J. Minár, S. Chadov, M. I. Katsnelson, H. Ebert, and A. I. Lichtenstein, Phys. Rev. B **79**, 115111 (2009).

[17] A. Glensk, B. Grabowski, T. Hickel, and J. Neugebauer, Phys. Rev. Lett. **114**, 195901 (2015).

[18] B. Grabowski, L. Ismer, T. Hickel, and J. Neugebauer, Phys. Rev. B **79**, 134106 (2009).

[19] X. Zhang, B. Grabowski, F. Körmann, C. Freysoldt, and J. Neugebauer, Phys. Rev. B **95**, 165126 (2017).

[20] F. Körmann, B. Grabowski, P. Söderlind, M. Palumbo, S. G. Fries, T. Hickel, and J. Neugebauer, J. Phys.: Condens. Matter **25**, 425401 (2013).

[21] O. Hellman, P. Steneteg, I. A. Abrikosov, and S. I. Simak, Phys. Rev. B **87**, 104111 (2013).

[22] I. A. Abrikosov, A. V. Ponomareva, P. Steneteg, S. A. Barannikova, and B. Alling, Curr. Opin. Solid State Mater. Sci. **20**, 85 (2016).

[23] S. Bigdeli, Developing the third generation of Calphad databases: What can ab-initio contribute?, Ph.D. thesis, KTH Royal Institute of Technology, 2017.

[24] A. I. Duff, T. Davey, D. Korbmacher, A. Glensk, B. Grabowski, J. Neugebauer, and M. M. W. Finnis, Phys. Rev. B **91**, 214311 (2015).

[25] P. Hohenberg and W. Kohn, Phys. Rev. **136**, B864 (1967).

[26] L. Vitos, H. L. Skriver, B. Johansson, and J. Kollar, Comput. Mater. Sci. **18**, 24 (2000).

[27] L. Vitos, Phys. Rev. B **64**, 014107 (2001).

[28] L. Vitos, I. A. Abrikosov, and B. Johansson, Phys. Rev. Lett. **87**, 156401 (2001).

[29] P. Soven, Phys. Rev. **156**, 809 (1967).

[30] B. L. Gyorffy, Phys. Rev. B **5**, 2382 (1972).

[31] J. Staunton, B. Gyorffy, A. Pindor, G. Stocks, and H. Winter, J. Magn. Magn. Mater. **45**, 15 (1984).

[32] J. Staunton, B. L. Gyorffy, A. J. Pindor, G. M. Stocks, and H. Winter, J. Phys. F **15**, 1387 (1985).

[33] Y. Wang and J. P. Perdew, Phys. Rev. B **44**, 13298 (1991).

[34] J. P. Perdew, J. A. Chevary, S. H. Vosko, K. A. Jackson, M. R. Pederson, D. J. Singh, and C. Fiolhais, Phys. Rev. B **46**, 6671 (1992).

[35] L. Vitos, *Computational Quantum Mechanics for Materials Engineers* (Springer-Verlag, London, 2007).

[36] H. J. Monkhorst and J. D. Pack, Phys. Rev. B **13**, 5188 (1976).

[37] A. V. Ruban and I. A. Abrikosov, Rep. Prog. Phys. **71**, 046501 (2008).

[38] D. Ma, B. Grabowski, F. Körmann, J. Neugebauer, and D. Raabe, Acta Mater. **100**, 90 (2015).

[39] Z. Li, F. Körmann, B. Grabowski, J. Neugebauer, and D. Raabe, Acta Mater. **136**, 262 (2017).

[40] B. Alling, F. Körmann, B. Grabowski, A. Glensk, I. A. Abrikosov, and J. Neugebauer, Phys. Rev. B **93**, 224411 (2016).

[41] N. D. Mermin, Phys. Rev. **137**, A1441 (1965).

[42] J. B. Staunton and B. L. Gyorffy, Phys. Rev. Lett. **69**, 371 (1992).

[43] L. Landau and E. Lifshitz, *Statistical Physics*, Course of Theoretical Physics No. 5 (Elsevier Science, Oxford, 2013).

[44] L. Bergqvist and A. Bergman, Phys. Rev. Materials **2**, 013802 (2018).

[45] A. V. Ruban, A. B. Belonoshko, and N. V. Skorodumova, Phys. Rev. B **87**, 014405 (2013).

[46] O. L. Anderson, in *Physical Acoustics*, Vol. III.-B, edited by W. P. Manson (Academic, New York, 1965), pp. 43–95.

[47] Z. S. Basinski and J. W. Christian, Proc. R. Soc. London A: Math. Phys. Sci. **223**, 554 (1954).

[48] H. Ehteshami and P. A. Korzhavyi, Phys. Rev. Materials **1**, 073803 (2017).

[49] H. Ehteshami and P. A. Korzhavyi, Phys. Rev. B **96**, 224406 (2017).

[50] H. M. Ledbetter, J. Appl. Phys. **44**, 1451 (1973).

[51] L. Landau, E. Lifshitz, A. Kosevich, and L. Pitaevskii, *Theory of Elasticity*, Course of Theoretical Physics No. 7 (Butterworth-Heinemann, Oxford, 1986).

[52] G. Grimvall, *Thermophysical Properties of Materials*, 1st ed. (Elsevier, North-Holland, 1999).

[53] P. Desai, J. Phys. Chem. Ref. Data **16**, 91 (1987).

[54] V. I. Razumovsky, A. V. Ruban, and P. A. Korzhavyi, Phys. Rev. Lett. **107**, 205504 (2011).